

# Shack-Hartmann wavefront sensing using interferometric focusing of light onto guide-stars

Xiaodong Tao,<sup>1,\*</sup> Ziah Dean,<sup>2</sup> Christopher Chien,<sup>3</sup> Oscar Azucena,<sup>1</sup> Dare Bodington,<sup>4</sup>  
and Joel Kubby<sup>1</sup>

<sup>1</sup>Department of Electrical Engineering, University of California, Santa Cruz, 1156 High St., Santa Cruz, California 95064, USA;

<sup>2</sup>Department of Biophysics, University of Michigan, 930 N. University Ave., Ann Arbor, Michigan 48109, USA;

<sup>3</sup>Department of Biology, University of California, Santa Cruz, 1156 High St., Santa Cruz, California 95064, USA;

<sup>4</sup>The Institute of Optics, University of Rochester, Rochester, New York 14627, USA

\*xiaod.tao@gmail.com

**Abstract:** Optical microscopy provides noninvasive imaging of biological tissues at subcellular level. The optical aberrations induced by the inhomogeneous refractive index of biological samples limits the resolution and can decrease the penetration depth. To compensate refractive aberrations, adaptive optics with Shack-Hartmann wavefront sensing has been used in microscopes. Wavefront measurement requires light from a guide-star inside of the sample. The scattering effect limits the intensity of the guide-star, hence reducing the signal to noise ratio of the wavefront measurement. In this paper, we demonstrate the use of interferometric focusing of excitation light onto a guide-star embedded deeply in tissue to increase its fluorescent intensity, thus overcoming the excitation signal loss caused by scattering. With interferometric focusing, we more than doubled the signal to noise ratio of the laser guide-star through scattering tissue as well as potentially extend the imaging depth through using AO microscopy.

©2013 Optical Society of America

**OCIS codes:** (110.1080) Active or adaptive optics; (010.7350) Wave-front sensing; (180.2520) Fluorescence microscopy; (170.3880) Medical and biological imaging.

---

## References and links

1. J. A. Kubby, *Adaptive Optics for Biological Imaging*, (CRC Press, 2013).
2. D. Débarre, E. J. Botcherby, T. Watanabe, S. Srinivas, M. J. Booth, and T. Wilson, "Image-based adaptive optics for two-photon microscopy," *Opt. Lett.* **34**(16), 2495–2497 (2009).
3. P. Marsh, D. Burns, and J. Girkin, "Practical implementation of adaptive optics in multiphoton microscopy," *Opt. Express* **11**(10), 1123–1130 (2003).
4. O. Albert, L. Sherman, G. Mourou, T. B. Norris, and G. Vdovin, "Smart microscope: an adaptive optics learning system for aberration correction in multiphoton confocal microscopy," *Opt. Lett.* **25**(1), 52–54 (2000).
5. X. Tao, B. Fernandez, O. Azucena, M. Fu, D. Garcia, Y. Zuo, D. C. Chen, and J. Kubby, "Adaptive optics confocal microscopy using direct wavefront sensing," *Opt. Lett.* **36**(7), 1062–1064 (2011).
6. X. Tao, J. Crest, S. Kotadia, O. Azucena, D. C. Chen, W. Sullivan, and J. Kubby, "Live imaging using adaptive optics with fluorescent protein guide-stars," *Opt. Express* **20**(14), 15969–15982 (2012).
7. M. Rueckel, J. A. Mack-Bucher, and W. Denk, "Adaptive wavefront correction in two-photon microscopy using coherence-gated wavefront sensing," *Proc. Natl. Acad. Sci. U.S.A.* **103**(46), 17137–17142 (2006).
8. N. Ji, D. E. Milkie, and E. Betzig, "Adaptive optics via pupil segmentation for high-resolution imaging in biological tissues," *Nat. Methods* **7**(2), 141–147 (2010).
9. M. J. Booth, M. A. Neil, R. Juskaitis, and T. Wilson, "Adaptive aberration correction in a confocal microscope," *Proc. Natl. Acad. Sci. U.S.A.* **99**(9), 5788–5792 (2002).
10. J. R. Mourant, J. P. Freyer, A. H. Hielscher, A. A. Eick, D. Shen, and T. M. Johnson, "Mechanisms of Light Scattering from Biological Cells Relevant to Noninvasive Optical-Tissue Diagnostics," *Appl. Opt.* **37**(16), 3586–3593 (1998).
11. Z. Yaqoob, D. Psaltis, M. S. Feld, and C. Yang, "Optical phase conjugation for turbidity suppression in biological samples," *Nat. Photonics* **2**(2), 110–115 (2008).
12. X. Xu, H. Liu, and L. V. Wang, "Time-reversed ultrasonically encoded optical focusing into scattering media," *Nat. Photonics* **5**(3), 154–157 (2011).
13. K. Si, R. Fiolka, and M. Cui, "Fluorescence imaging beyond the ballistic regime by ultrasound pulse guided digital phase conjugation," *Nat. Photonics* **6**(10), 657–661 (2012).

14. B. Judkewitz, Y. M. Wang, R. Horstmeyer, A. Mathy, and C. Yang, "Speckle-scale focusing in the diffusive regime with time-reversal of variance-encoded light (TROVE)," *Nat. Photonics* **7**(4), 300–305 (2013).
15. I. M. Vellekoop, E. G. van Putten, A. Lagendijk, and A. P. Mosk, "Demixing light paths inside disordered metamaterials," *Opt. Express* **16**(1), 67–80 (2008).
16. I. M. Vellekoop, A. Lagendijk, and A. P. Mosk, "Exploiting disorder for perfect focusing," *Nat. Photonics* **4**(5), 320–322 (2010).
17. D. B. Conkey, A. N. Brown, A. M. Caravaca-Aguirre, and R. Piestun, "Genetic algorithm optimization for focusing through turbid media in noisy environments," *Opt. Express* **20**(5), 4840–4849 (2012).
18. M. Cui, "A high speed wavefront determination method based on spatial frequency modulations for focusing light through random scattering media," *Opt. Express* **19**(4), 2989–2995 (2011).
19. R. Fiolka, K. Si, and M. Cui, "Parallel wavefront measurements in ultrasound pulse guided digital phase conjugation," *Opt. Express* **20**(22), 24827–24834 (2012).
20. D. B. Conkey, A. M. Caravaca-Aguirre, and R. Piestun, "High-speed scattering medium characterization with application to focusing light through turbid media," *Opt. Express* **20**(2), 1733–1740 (2012).
21. C. Stockbridge, Y. Lu, J. Moore, S. Hoffman, R. Paxman, K. Toussaint, and T. Bifano, "Focusing through dynamic scattering media," *Opt. Express* **20**(14), 15086–15092 (2012).
22. M. Gu, *Advanced Optical Imaging Theory* (Springer-Verlag, New York, 1999).
23. E. Chaigneau, A. J. Wright, S. P. Poland, J. M. Girkin, and R. A. Silver, "Impact of wavefront distortion and scattering on 2-photon microscopy in mammalian brain tissue," *Opt. Express* **19**(23), 22755–22774 (2011).
24. E. G. van Putten, I. M. Vellekoop, and A. P. Mosk, "Spatial amplitude and phase modulation using commercial twisted nematic LCDs," *Appl. Opt.* **47**(12), 2076–2081 (2008).
25. D. Malacara, *Optical Shop Testing*, (Wiley, New York, 2007).
26. M. A. Schofield and Y. Zhu, "Fast phase unwrapping algorithm for interferometric applications," *Opt. Lett.* **28**(14), 1194–1196 (2003).
27. I. Vellekoop and C. Aegerter, "Focusing light through living tissue," *Proc. SPIE* **7554**, 755430 (2010).
28. N. Ji, D. E. Milkie, and E. Betzig, "Adaptive optics via pupil segmentation for high-resolution imaging in biological tissues," *Nat. Methods* **7**(2), 141–147 (2010).
29. I. M. Vellekoop, "Controlling the Propagation of Light in Disordered Scattering Media," PhD thesis, Univ. Twente (2008).
30. J. Porter, H. Queener, J. Lin, K. Thorn, and A. A. S. Awwal, *Adaptive Optics for Vision Science: Principles, Practices, Design and Applications*, (Wiley, 2006).
31. J. W. Hardy, *Adaptive Optics for Astronomical Telescopes* (Oxford University Press, 1998).
32. J. Tang, R. N. Germain, and M. Cui, "Superpenetration optical microscopy by iterative multiphoton adaptive compensation technique," *Proc. Natl. Acad. Sci. U.S.A.* **109**(22), 8434–8439 (2012).

---

## 1. Introduction

With the advantages of high-resolution and viewing of live organisms, optical microscopy has become an important tool for biological research and continues to open new avenues in its capabilities. In recent years, image resolution and speed has been dramatically improved. However the improvement of the resolution and penetration depth for optical microscopy is still in its infancy. As light passes through biological tissue, it can be absorbed, refracted and scattered, limiting the resolution and depth of optical imaging in biological tissues. Overcoming these challenges will benefit a wide range of applications from basic biological research to clinical investigations. To correct the refractive aberration, Adaptive Optics (AO) with different strategies has been applied in optical microscopes [1]. The indirect wavefront sensing method was first applied in an AO system to retrieve the optimal phase by maximizing the detected signal from samples [2–4]. Numerous iterations are required to find the wavefront, causing photobleaching while limiting the bandwidth of imaging. The direct wavefront sensing method often applies a Shack-Hartmann wavefront sensor (SHWS) or interferometer to measure the wavefront directly using the light from a fluorescent microsphere [5], fluorescent proteins [6], or backscattered light from the samples [7]. Other approaches use a direct wavefront measurement based on sequential measurements of the wavefront error in each segment of the aperture [8], or sequential intensity measurements with different trial aberrations [9]. In all of the above methods, the performance relies heavily on the intensity of the ballistic light from the samples. In biological tissues, the ballistic light will be attenuated exponentially with increasing depth because of scattering. When using Shack-Hartmann wavefront sensing, the scattering will not only limit the amount of photons delivered to the guide-star, but also increase the background noise of neighboring guide-stars. Both of these effects reduce the signal to noise ratio (SNR) for wavefront measurements.

Scattering is caused by inhomogeneities in biological tissues. The majority of scattered light from a cell is due to the nucleus and smaller organelles such as mitochondria [10]. The

amplitude of elastic scattering loss is noted to be an order of magnitude or more than that of absorption. Although scattering is entirely random, it is a deterministic and time reversible process. The optical phase conjugation (OPC) method has been successfully applied to measure the phase and amplitude of the scattered light field, retrace its trajectory through the scattering medium and recover its original input light field [11]. To measure the light field coming from the observed area, OPC needs coherent light from the area of interest. Meanwhile, in a recent study, ultrasonically encoded focusing has been utilized to generate a guide-star as a coherent point source for phase measurement [12–14]. Another method, called interferometric focusing (IF), is also used to estimate the optimal phase of the scattering light field by modulating the phase of illumination light while analyzing the variation of emission light from the sample [15, 16]. By measuring the phase of scattered light from the point source in the sample one can match the scattering behavior of the turbid material and as a result allow constructive interference to occur, thereby increasing intensity at the point source. In conventional focusing the paths of light rays are determined by Fermat's principle of least time; light will take a path between two points that minimizes the travel time. Interferometric focusing uses the coherent properties of light to cause constructive interference at the focus and this is done by adjusting the phase of each scattering channel to obtain constructive interference at the bead [15]. To increase the speed of the phase estimation, different methods have been applied, such as a genetic algorithm, spatial frequency modulation and parallel wavefront optimization methods [17–19]. Fast light modulators, such as the Digital Micromirror Device (DMD) from Texas Instruments and segmented deformable mirrors from Boston Micromachines, have also been used to further speed up the optimization process [20, 21].

Although scattering will exponentially reduce the intensity of ballistic light with the imaging increasing depth, correction of refractive aberration still benefits the imaging resolution and contrast. For two-photon imaging of mouse brain tissue, it has been shown that wavefront distortions are the main factor for enlargement and distortion of the point spread function (PSF) [22] at intermediate imaging depths [23]. Wavefront correction can dramatically reduce the surrounding lobes of the PSF in the brain tissues. The advantages of the large isoplanatic angle and fast correction speed make it suitable for live imaging. This paper demonstrates the use of the IF method, rather than conventional geometric focusing to concentrate excitation light onto a guide-star in tissue for direct wavefront measurement using a SHWS. Interferometric focusing can increase the fluorescent intensity of the guide-star, thus overcoming signal loss caused by scattering. By minimizing scattering, less power is required to generate a guide-star bright enough for wavefront measurement. The wavefront can be measured by a SHWS with fluorescence from the illuminated laser guide-star. These measurements will subsequently be used in our AO microscope to overcome refractive image aberrations using adaptive geometric optics. With the IF of light, we will double the illumination of the laser guide-star through scattering tissue and potentially double the thickness of tissue that can be corrected using AO microscopy. In addition, the correction of the refractive aberration when using AO provides a larger correction field, compared to the scattering compensation while using IF.

## 2. Method

### 2.1 System layout

Figure 1 shows the configuration of the system. A HeNe laser (LHX1, CVI Melles Griot) was used as the excitation source. The beam was further expanded by lenses L1 and L2, which covers an area with a radius of 4mm on a reflective spatial light modulator (SLM) (LC-R 2500, Holoeye). The excitation light passes through two polarizers, P1 and P2, for intensity adjustments and setting the polarization angle of the incident beam on the SLM. A half-wave plate after the polarizer allows adjustment of the polarization angle without changing the intensity of the laser. The SLM is located between an analyzer and a half-wave plate. With a spatial filter and multi-pixel combination, the phase and amplitude of light reflected from the

SLM can be controlled independently [24]. Here we only adjust the phase of the reflected light. In order to calibrate the SLM input vs. phase relationship, a phase shifting interferometer is integrated into the system. The reference mirror is installed on a piezo-actuated nano-positioning stage (17MAX301, Melles Griot) in order to introduce a precise phase shift. The reference beam and the measurement beam from the SLM are combined by a beam splitter, so when interference takes place, interference fringes are formed. The interference pattern is projected on to a CCD camera by lens L4. The surface of the SLM is conjugate to the front surface of the CCD plane. The phase of the SLM can then be obtained using the Hariharan algorithm and unwrapped by a discrete cosine transformation based on the phase-unwrapping algorithm [25, 26]. The calibration system can both register the location of the pupil and be used for displaying the measured wavefront on the SLM. The calibration system can be switched from the main system by a flipper mirror F1. The modulated beam is focused on the sample through a 60X water immersion objective with a numerical aperture of 1.1 (Olympus Microscope, Center Valley, PA). Lenses L3 and L5 image the exit pupil of the objective on to the SLM. The emission light is separated from the excitation light by a dichroic beam splitter DB. After passing through an emission filter, the modulated emission light is finally detected by an electron multiplying CCD (EMCCD) camera (Cascade II:512, Photometrics) for the optimization of the scattered light field phase. After the optimal input phase is determined, the flipper mirror (F2) is switched up to direct light through a second emission filter (E2) and onto the wavefront sensor, which is composed of a  $11 \times 11$  element lenslet array (AOA Inc., Cambridge, MA), with a lenslet diameter of  $400 \mu\text{m}$  and a focal length of 24 mm and a CCD camera (M1400, Dalsa). The pitch of the lenslet array is  $400 \mu\text{m}$ . The spatial filter SF2 is used to reject scattered and background light. The size of SF2 is chosen based on the highest spatial frequency that was detectable with the wavefront sensor [1]. In our system, a pinhole with diameter of  $400 \mu\text{m}$  is used which corresponds to a minimum spatial period of  $800 \mu\text{m}$  on the aperture of the wavefront sensor. The sample is installed on a nano-positioning stage (NanoMax, Thorlabs) for precise alignment of the bead.

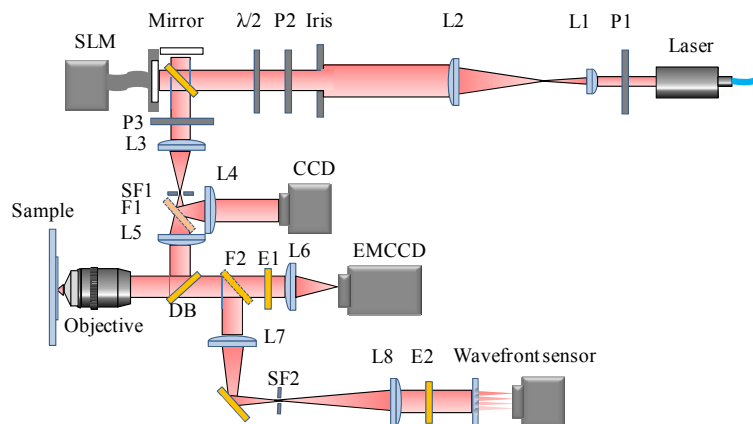


Fig. 1. System layout for testing IF of light on to a guide-star: A He-Ne laser emits light at 633 nm for excitation of a fluorescent reference beacon. The laser is modulated by a spatial light modulator (SLM) and generates interferometric focusing at the guide-star by an optimization process using the intensity information from an EMCCD camera. The emission light from the enhanced guide-star feeds into a SH wavefront sensor for direct wavefront measurement. L, lens; F, flipper mirror; P, polarizer; DB, dichroic beamplitters; E, emission filter; SF, spatial filter.

In the system, the pupil on the SLM is divided into 316 square segments, which is conjugate to the exit pupil of the objective. The phase of each segment is modulated independently by the SLM. The emission light from the target is collected by the EMCCD.

The sum of the intensity of 20x20 pixels around the target on the image was calculated as the intensity measurement. The step-wise optimization was performed to retrieve the best phase [15]. For each segment, the phase changes from 0 to  $2\pi$  in 5 steps. The best phase is calculated by fitting intensity measurements for these 5 steps with a sinusoid function. The optimal phase for the current segment is updated before advancing to the next segment. Operation time is mainly limited by the response time of the SLM, which is 80 ms in the current setup. The exposure time for EMCCD is set as 20 ms. A full compensation takes 158s. Longer operation times will expose the sample to potential photobleaching and photodamage. For live samples, the extended operation time also causes the loss of IF because of the dynamic change of optical properties and the drift of the stage [27]. By using fast modulators, such as a DMD [20] or a segmented MEMS deformable mirror [21], more segments can be used in a shorter amount of time. Because the intensity gain is proportional to the number of the segments, fast modulators will dramatically improve the performance for imaging of live samples.

## 2.2 IF of light onto guide-stars

Most of the wavefront correction methods used in microscopy are based on probing either fluorescent or backscattered light from the sample for wavefront measurement using a wavefront sensor and a guide-star or indirect phase optimization [1]. However attenuation of the excitation light caused by scattering will decrease the SNR and degrade the system performance. Increasing the laser power will lead to photo-bleaching and photo-damage of the sample and further increase background noise. A promising solution to overcome these issues is IF of concentrated light onto guide-stars for wavefront measurements, such as a fluorescent microsphere or protein. Focusing light through scattering tissue can be achieved when light interferes constructively at the target [15, 16]. Only one guide-star inside of the scattering tissue needs to be illuminated for each wavefront measurement. By using fast light modulators, such as the Digital Micromirror Device (DMD) from Texas Instruments, the total operation time can be less than one second, which is acceptable for most of imaging situations [20].

To quantify the system performance, the excitation distribution on the guide-star can be calculated as:

$$I_{GS}(x, y) = |h_{psf}(x, y)|^2 f_{flou}(x, y) \quad (1)$$

where  $h_{psf}$  is the PSF at the focal plane.  $f_{flou}$  is the fluorophore distribution at the focal plane. Here we neglect fluorescence from out of focus planes by assuming that it can be blocked by the spatial filter (SF2) as shown in Fig. 1.  $f_{flou}$  can be simplified as a circular function where a microsphere with a radius of  $r_b$  is used as guide-star, giving:

$$f_{flou}(x, y) = \begin{cases} \alpha & \text{for } \sqrt{x^2 + y^2} \leq r_b \\ 0 & \text{otherwise} \end{cases} \quad (2)$$

where  $\alpha$  is a scaling factor. The PSF is defined as [22]:

$$h(x_2, y_2) = \frac{i}{\lambda} \iint_{\Sigma} P(x_1, y_1) \exp[-ik\phi(x_1, y_1)] \frac{\exp[-ik(r-R)]}{Rr} \cos(n, r) dS_p \quad (3)$$

where  $(x_2, y_2)$  are the coordinates in the focusing plane.  $(x_1, y_1)$  are the coordinates in the pupil plane.  $P(x_1, y_1)$  and  $\phi(x_1, y_1)$  are the light field in amplitude and phase, respectively.  $k$  is the wave number.  $n$  is the unit normal of the pupil plane.  $r$  is the unit vector from  $(x_1, y_1)$  to  $(x_2, y_2)$ .  $R$  is the distance from the pupil plane to  $(x_2, y_2)$ .  $dS_p$  is the area element on the pupil plane.  $\lambda$  is the wavelength of the illumination light. To take into account the exponential intensity attenuation caused by scattering, the pupil function can be calculated as [23]:

$$P(x, y) = e^{-\left(\frac{z_p}{2L_{se} \cos(n, r)}\right)} \quad (4)$$

where  $z_p$  is the depth of the guide-star.  $L_{se}$  is the mean free path (MFP). For simplicity, we assume the pupil is illuminated evenly. Substituting Eq. (4) and Eq. (3) into Eq. (1) leads to the intensity of the guide-star inside of the tissue. Because the wavefront sensor collects the ballistic light from the guide-star, Eq. (4) is only satisfied when scattering of either excitation or emission light is fully compensated. Without any compensation, the square of the pupil function should be used instead.

Here we use a fluorescent microsphere with a diameter of 1  $\mu\text{m}$  as guide-star. The wavefront,  $\varphi$ , of mouse brain tissue with a thickness of 100  $\mu\text{m}$  is measured using the SH wavefront sensor. In the simulation, we assume the amplitude of the wavefront is proportional to the depth of the tissue, which is in accordance to the real measurement [28]. To measure the MFP of the mouse brain tissue, brain slices with thicknesses of 100  $\mu\text{m}$ , 150  $\mu\text{m}$  and 200  $\mu\text{m}$  are prepared. Images of a fluorescent microsphere under the tissue are captured. By using the method described in [23], the MFP is measured as 30.82  $\mu\text{m}$  with 95% confidence bounds of 29.12  $\mu\text{m}$  and 32.74  $\mu\text{m}$ . Next the normalized intensity of the guide-star was calculated in three circumstances: when there is only aberration, aberration with single path scattering and aberration with double path scattering, as shown in Fig. 2. As can be seen, the intensity of the guide-star decreases exponentially with the imaging depth. At a depth of 100  $\mu\text{m}$ , the intensity of a guide-star with double path scattering is around 0.1% of the one without scattering. In the case of perfect phase conjugation for compensation of the scattering in excitation light, the intensity of the guide-star can be increased by 5 times at a depth of 50  $\mu\text{m}$ . In the real situation, the improvement by IF is limited by a variety of factors, such as the finite size of the modulator, the limited resolution of the modulated phase and phase only modulation [29]. Because the depth of the guide-star in the sample is within several MFPs, the intensity improvement is moderate compared with the results for more highly scattering samples [15, 16]. Although most of the attenuation is caused by scattering, correction of the aberration alone can increase the intensity by nearly two times and the Strehl ratio, where it is defined by the ratio of peak intensities in the aberrated and ideal PSF [1], by nearly five times at a depth of 100  $\mu\text{m}$ .

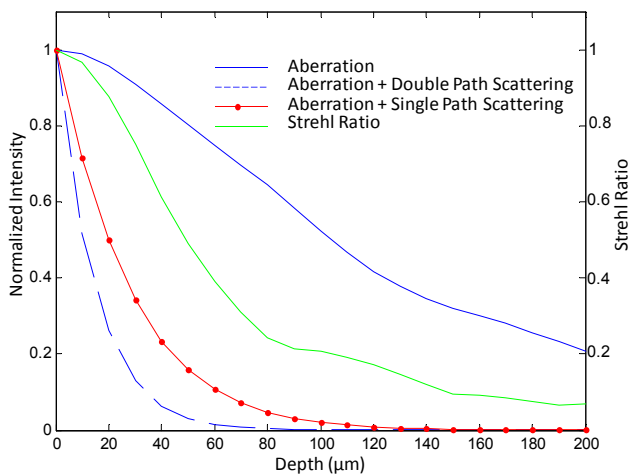


Fig. 2. Modeling the intensity of guide-stars with aberration (blue solid line), aberration and double path scattering (blue dashed line), aberration and single path scattering (red line) and the Strehl ratio (green solid line).

### 2.3 Wavefront measurement

The emission light from the guide-star was detected by a SHWS with a 11x11 lenslet array. It can make a reliable measurement of an aberration up to the first 97 Zernike modes [1], which is high enough for correcting refractive aberrations in most biological tissues. Before wavefront measurement, a reference pattern is recorded with collimated light fed into the system. During measurement, the slope of the wavefront on each sub-aperture was calculated by the displacement of the spot on the wavefront sensor. Then the wavefront is reconstructed by the vector-matrix-multiplication (VMM) method [30]. The measurement noise of the wavefront sensor is related to the signal to noise ratio (SNR) of the camera, which can be estimated using [31]:

$$\sigma_m = \sqrt{2} \frac{\pi^2 K_g}{4(SNR)} \left[ \left( \frac{3}{2} \right)^2 + \left( \frac{\theta d}{\lambda} \right)^2 \right] \quad (5)$$

where  $K_g$  is a constant to account for centroiding errors due to the fill factor on the CCD,  $\theta$  is the angular radius of the spot size,  $\lambda$  is the wavelength of the excitation light and  $d$  is the sub-aperture diameter. The signal to noise ratio of the detector is given by:

$$SNR = \frac{n_p}{\sqrt{n_p + N_D[n_B^2 + (e/G)^2]}} \quad (6)$$

where  $n_p$  is the number of detected photoelectrons per sub-aperture,  $N_D$  is the number of detector pixels per sub-aperture.  $n_B$  is the number of detected background electrons per pixel,  $e$  is the read noise and  $G$  is the intensifier gain.

### 2.4 Sample preparation

Fixed brain slices from a YFP-M line transgenic mouse were prepared. Brain coronal sample sections each at a thickness of 50  $\mu\text{m}$ , 75  $\mu\text{m}$  and 100  $\mu\text{m}$  were cut with a microtome. The samples were kept in Phosphate Buffered Saline (PBS) solution and stored at 4  $^\circ\text{C}$  until use. One micrometer diameter crimson fluorescent microspheres (Invitrogen, Carlsbad, CA) were deposited onto a glass slide and a cover plate for use as laser guide-stars. Custom-made chambers were made on the glass slides for mounting the thick tissues. Before measurement, the samples were mounted in a chamber with 5% agarose. To avoid changes in the optical properties caused by the evaporation of water from the sample, all the measurements were performed within 10 hours of mounting.

## 3. Experimental result

### 3.1 Measurement and correction of wavefront aberration in mouse brain tissues

Because the surface of the SLM is not perfectly flat, it leads to optical aberrations in the system. To compensate this system aberration, the phase induced from the SLM's surface was measured using a phase shifting interferometer, which has been integrated into the system. An opposite phase map, shown in Fig. 3(a) (bottom), was applied to the SLM in order to compensate its surface phase. The spherical aberration induced by the cover glass was initially compensated by adjusting a correction collar on the objective lens. To investigate the proposed method, we performed the wavefront measurement using IF of light onto the guide-star. First, the fluorescent microsphere at the bottom of the mouse brain tissue with a thickness of 100  $\mu\text{m}$  was illuminated by the laser with a wavelength of 633 nm using only the system correction. The image of the microsphere and the phase on the SLM are shown in Fig. 3(a) (top). The brightest intensity was achieved by precisely adjusting the position of the microsphere in a three dimensional space with respect to the objective using a nano-positioning stage. Then IF was performed to compensate scattering in the sample. A much brighter image was achieved as shown in Fig. 3(b) (top). The intensity increased two times.

The images from the wavefront sensor before and after IF are shown in Figs. 4(a)–(b), respectively. After IF, the SNR of the wavefront sensor increased from 41.88 to 83.70. The RMS error decreased from  $0.22 \lambda$  to  $0.11 \lambda$ . The intensity of the spots on the wavefront sensor more than doubled. The phase map after IF optimization is shown in Fig. 3(b) (bottom). The random phase corresponds to the suppression of the scattering effect from the diffuse light. The relatively smooth shape close to the center of the phase map is from wavefront error from ballistic light. Figure 3(c) (bottom) shows the wavefront error measured from the wavefront sensor. A similar shape as is seen on the SLM in Fig. 3(b) (bottom) can be observed on the wavefront error map determined by the SHWS shown in Fig. 3(c) (bottom). The phase image displayed on the SLM will contain both low-order and high-order corrections. The low-order corrections are expected to extend to a larger isoplanatic patch than the high-order corrections, so we are interested in obtaining the low-order corrections to correct a larger patch. It may be possible to separate out the low-order and high-order aberrations in the SLM instead of using the SHWS to determine the low-order aberration when the refractive aberration is the dominant factor. But when scattering becomes the dominant factor, separating them could be difficult because of the highly random phase for compensation of scattered light. An additional factor is that the light paths taken by photons traveling to the guide-star in IF determined by channel demixing [15] may be different than the light paths taken by ballistic photons that travel along paths determined by least travel time [1], so the low-order aberrations measured using the SLM and SHWS may be different since they could sample different volumes of the sample. The direct retrieval of the low-order aberrations from the phase image on the SLM with different amounts of scattering will be investigated in the future. The result will be compared with the aberrations measured by SHWS. The image of the microsphere after applying this wavefront measurement to the SLM is shown in Fig. 3(c) (top). The intensity increases 1.5 times compared with the image before wavefront correction in Fig. 3(a) (top). We also tested the proposed method for fixed brain tissues with variable thicknesses. Three fixed brain tissues were prepared with thicknesses of 60  $\mu\text{m}$ , 80  $\mu\text{m}$  and 100  $\mu\text{m}$ . The SNR improvement of the wavefront sensor and the intensity improvement of the image after wavefront correction are shown in Fig. 4(c). As can be seen, the intensity improvement follows a linear trend. The difference between these two improvements is from 0.013 at the image depth of 60  $\mu\text{m}$  to 0.418 at the depth of 100  $\mu\text{m}$ , because scattering effects become a more dominant factor for attenuation of the light for the thicker tissue.

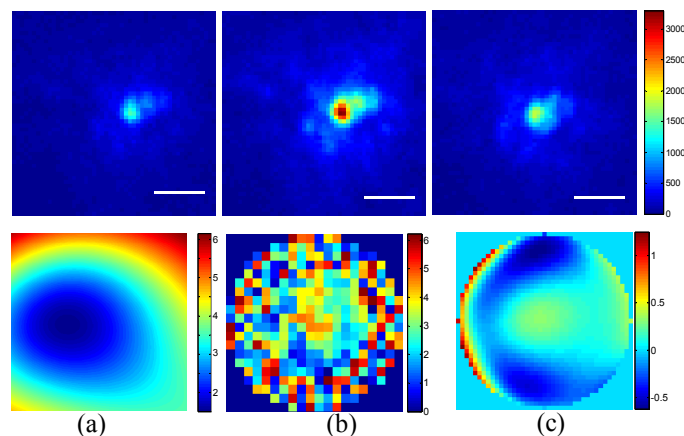


Fig. 3. A 1  $\mu\text{m}$  diameter fluorescent bead under a 100  $\mu\text{m}$  thick fixed mouse brain tissue sample used as a guide-star for wavefront measurement. (a) The image of the guide-star after compensation of system aberration (top) and the phase map displayed on the SLM (bottom). (b) The image of the guide-star after IF (top) and the phase map to compensate scattering (bottom). The intensity increases more than two times. (c) The image of the guide-star after refractive aberration correction (top) and the phase map measured from a SHWS (bottom). The scale bar is 2  $\mu\text{m}$ .

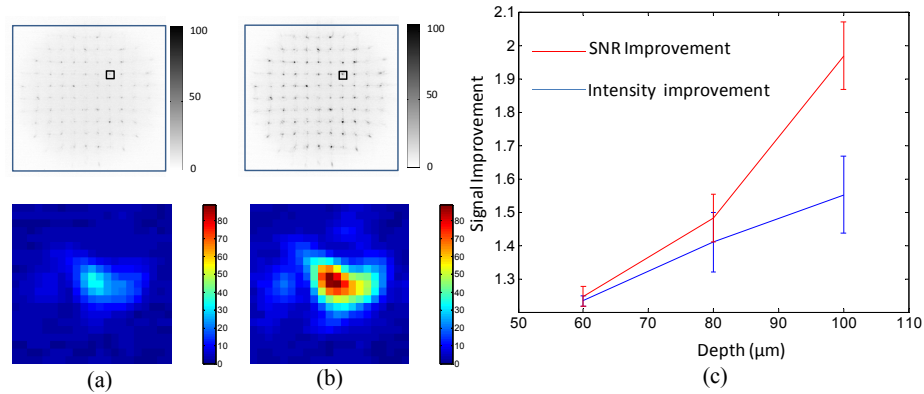


Fig. 4. Wavefront measurement results using IF guide-stars: Complete images from the SH wavefront sensor (grayscale inverted for clarity) and images of a single spot indicated by white square before (a) and after (b) IF. (c) The SNR improvement of wavefront measurement and intensity improvement for various depths. The error bars represent the standard deviation of the mean.

### 3.2 Noise suppression for multiple guide-stars

Another advantage of using IF to focus light onto a guide-star is the ability to eliminate the noise from neighboring guide-stars for wavefront measurement. The diffuse part of the excitation light increases the illumination area at the focal plane. If there are multiple guide-stars located inside of this area, the emission from the neighboring guide-stars will increase background noise for wavefront measurement. Figure 5(a) shows the image of multiple beads without compensation for scattering. The encircled energy from the center of the bead is calculated as shown in Fig. 5(e). The radius of the area containing 80% of energy is  $2.67 \mu\text{m}$ . It generates a significant noise on the wavefront sensor as shown in Fig. 5(c). After IF, the focus is much more concentrated as shown in Fig. 5(b). 80% of the energy is concentrated in an area with a radius of  $1.45 \mu\text{m}$ . The corresponding image of a spot from the wavefront sensor shows a much brighter spot with less background noise as shown in Fig. 5(d).

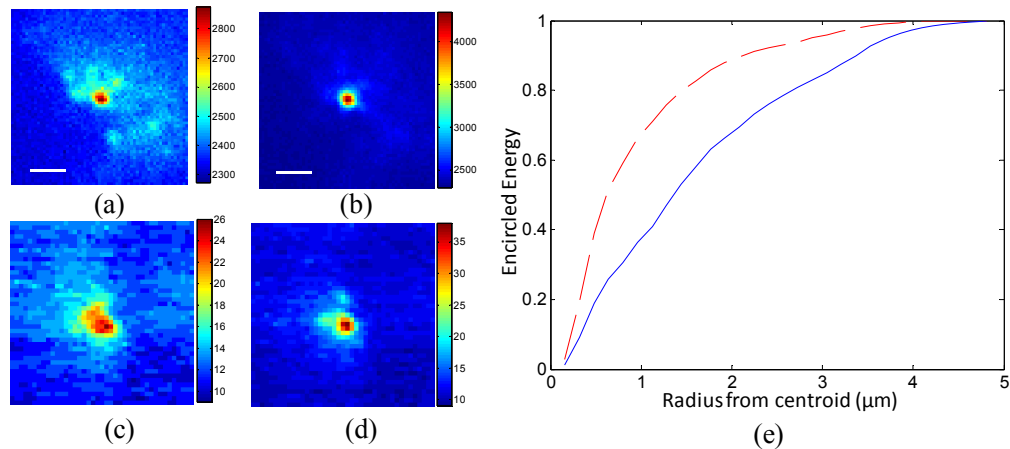


Fig. 5. Effects of multiple guide-stars: Images of multiple guide-stars before IF (a) and after IF (b). Spot images from the wavefront sensor before IF (c) and after IF (d). Encircled energy of the guide-star before (solid blue line) and after IF (dashed red line) (e). The scale bar is  $2 \mu\text{m}$ .

### 3.3 Spatial dependence of wavefront correction vs. scattering compensation

Although IF can dramatically increase the intensity of the excitation beam by compensation of scattering, the compensation is only valid in a very limited area. A time consuming process by stitching a number of small compensation patches to achieve a larger field of view (FOV) is required [32]. To compare the spatial dependence of these two methods, we tested them on a fixed mouse brain tissue with a thickness of 100  $\mu\text{m}$ . We first performed IF on a fluorescent microsphere and measured the refractive aberration using the SHWS. We then proceeded to move the sample across the FOV randomly four times using a manual micro-positioning stage. In each step, we captured images using the phase maps that were measured at the initial position using IF and SHWS respectively. We repeated those measurements five times. The starting positions for those five rounds of measurements were within a small area with a radius of 10  $\mu\text{m}$  and the same wavefront map was used for the correction of refractive aberration in all the measurements. The phase maps for IF at the initial position shown in Fig. 6(a) display a random phase distributed in each subaperture. The intensity of the microsphere dropped dramatically with an increase of the distance. By fitting a Gaussian curve to the measurement for IF shown as a green line in Fig. 6(a), the full width half maximum (FWHM) of the improvement is only 6.06  $\mu\text{m}$ . However, the improved correction of refractive aberration, within a distance of 20  $\mu\text{m}$ , using the phase map shown in Fig. 6(b), shows no significant change. This agrees with the results in [23]. The average of the improvement is 1.46.

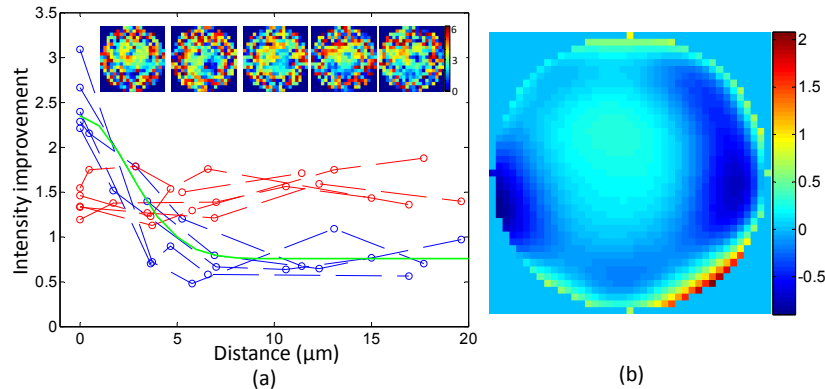


Fig. 6. Spatial dependence of wavefront correction and scattering compensation. (a) Intensity improvement at different places using the phase map for the refractive aberration correction (red dashed line) and scattering compensation (blue dashed line) at the initial position. The data for scattering compensation is fitted by a Gaussian function shown as the green curve. Phase maps show the optimal phase of IF at the initial position for five tests. (b) The phase map for compensation of the refractive aberration in all the tests. RMS error is  $0.32\lambda$ .

### Conclusion

In this paper, we have demonstrated that IF, rather than conventional geometric focusing, of excitation light onto a guide-star that is embedded deeply in tissue, increases its fluorescence intensity. The proposed method can extend the depth of wavefront measurement and improve correction inside of tissues because of its ability to suppress both scattering of diffuse light and aberration of ballistic light. The results showed more than two times improvement in SNR and RMS error of the wavefront measurement. Although only ballistic light in the excitation path is corrected, the intensity after wavefront correction increased by 1.5 times. Because the system setup is only used to verify the proposed wavefront sensing method, only the excitation light path was corrected. Further improvements can be achieved if both excitation and emission light paths are corrected. When applying IF to a two-photon

microscope with a near infra-red laser, this method would further extend the measurement depth and achieve high SNR for the wavefront sensor.

### **Acknowledgments**

The results presented herein were obtained at the W.M. Keck Center for Adaptive Optical Microscopy (CfAOM) at University of California Santa Cruz. The CfAOM was made possible by the generous financial support of the W.M. Keck Foundation. We would like to thank Prof. Yi Zuo and Dr. Eric Chen of MCD Biology at UCSC for the mouse tissue samples that were used in these experiments; Marc Reinig for valuable discussions. We also acknowledge the technical support from Ben Abrams in the UCSC Life Sciences Microscopy Center.